RESEARCH ARTICLE

Theoretical and experimental study on the fluidity performance of hard-to-fluidize carbon nanotubes-based CO$_2$ capture sorbents

Mahsa Javidi Nobarzad[1], **Maryam Tahmasebpoor** (✉)[1], **Mohammad Heidari**[1], **Covadonga Pevida** (✉)[2]

1 Faculty of Chemical & Petroleum Engineering, University of Tabriz, Tabriz 51666-16471, Iran
2 Instituto de Ciencia y Tecnología del Carbono, INCAR-CSIC, Oviedo 33011, Spain

Abstract Carbon nanotubes-based materials have been identified as promising sorbents for efficient CO$_2$ capture in fluidized beds, suffering from insufficient contact with CO$_2$ for the high-level CO$_2$ capture capacity. This study focuses on promoting the fluidizability of hard-to-fluidize pure and synthesized silica-coated amine-functionalized carbon nanotubes. The novel synthesized sorbent presents a superior sorption capacity of about 25 times higher than pure carbon nanotubes during 5 consecutive adsorption/regeneration cycles. The low-cost fluidizable-SiO$_2$ nanoparticles are used as assistant material to improve the fluidity of carbon nanotubes-based sorbents. Results reveal that a minimum amount of 7.5 and 5 wt% SiO$_2$ nanoparticles are required to achieve an agglomerate particulate fluidization behavior for pure and synthesized carbon nanotubes, respectively. Pure carbon nanotubes + 7.5 wt% SiO$_2$ and synthesized carbon nanotubes + 5 wt% SiO$_2$ indicates an agglomerate particulate fluidization characteristic, including the high-level bed expansion ratio, low minimum fluidization velocity (1.5 and 1.6 cm·s^{-1}), high Richardson−Zaki *n* index (5.2 and 5.3 > 5), and low Π value (83.2 and 84.8 < 100, respectively). Chemical modification of carbon nanotubes causes not only enhanced CO$_2$ uptake capacity but also decreases the required amount of silica additive to reach a homogeneous fluidization behavior for synthesized carbon nanotubes sorbent.

Keywords CO$_2$ capture, CNT-based sorbents, fluidization, SiO$_2$ nanoparticles, fluidized bed reactors

1 Introduction

To limit the CO$_2$ emissions which arise from the burning of large volumes of fossil fuels to satisfy the increasing energy demand, significant efforts and investigations have been devoted to developing CO$_2$ capture and storage technologies [1,2]. Among all the proposed alternatives, e.g., membrane [3], absorption [4], adsorption [5], etc., the development of promising solid sorbents, e.g., zeolites [6], MgO [7], alkali-based [8], carbon nanotube (CNT) [9], CaO [10], metal-organic frameworks [11,12], etc. with good adsorption/regeneration and superior regeneration properties has received more attention recently as a potentially inexpensive technique. CNTs are sufficient candidates owing to their fluffy tubular structure, large surface area, high thermal and chemical stability, unique pore structure, high mechanical strength, low-temperature adsorption and regeneration, and promising performance in prolonged cycling [13]. In this regard, CNTs have been reported as appropriate candidates for CO$_2$ sorption processes. For instance, 22.7 mg of CO$_2$ were adsorbed on the surface of 1 g raw CNT, demonstrating the significant capability of CNTs to adsorb CO$_2$ [14]. To strengthen the CO$_2$ affinity of CNTs, they are usually modified with amino-containing compounds to increase the alkaline group content on the surface and then reach high CO$_2$ capture levels. According to the study by Lu et al. [14], the CNTs possess the highest adsorption capacity of CO$_2$ under the same test conditions compared to zeolites and granular activated carbon after amine functionalization. The modification of pure CNT with monoethanolamine (MEA) resulted in an 18.5% increase in the equilibrium amount of adsorbed CO$_2$ compared to raw CNT. Recent research indicated that adding 70 wt% silica to pure CNT grafted with 20 wt% polyethylenimine resulted in a CO$_2$ uptake of 84.48 mg·g^{-1} of sorbent. It

was a 10.9% increase compared to the similar sample without silica in the structure [13]. This demonstrates the effectiveness of silica addition to boost the performance of amino-containing CNT-based sorbents for CO_2 adsorption via decreasing agglomeration. Morphology and surface modification of nanoparticles (NPs) via incorporation into additives to diminish agglomeration and improve characteristics has been widely evaluated [15–17].

In addition to their high adsorption capacity, the proper fluidity of solid CO_2 sorbents also plays a vital role in selecting the most suitable sorbent for practical applications. This means that an efficient contact between the CO_2 gas and the solid sorbent is essential to increase the CO_2 capture capacity. Recently, many research studies have been accomplished in fluidized bed reactors due to their wide application for industrial chemical processes dependent strongly on the fluidization performance of sorbent [18].

The main characteristics of nanopowders are their cohesive nature due to the strong interparticle forces such as van der Waals, electrostatic, and capillary, which lead to the formation of durable particle agglomerates [19,20]. The CNTs are generally in the range of 100–200 nm in diameter and 5–20 microns in length. The enlarged length of CNTs intensifies the tendency of CNTs to become entangled and form large agglomerates. In addition to the high aspect ratio, the CNTs synthesis methods also produce entangled forms. The low bending rigidity of CNTs further leads to their aggregation. CNTs aggregation further becomes strengthened due to van der Waals forces [21]. These agglomerates exhibit two disparate types of fluidization behavior, i.e., agglomerate particulate fluidization (APF) and agglomerate bubbling fluidization (ABF) [22]. The APF behavior is characterized by very smooth and bubble-less fluidity accompanied by remarkably high bed expansion and low minimum fluidization velocity (U_{mf}). For the NPs showing ABF behavior, fluidization results in a minimal bed expansion accompanied by a high U_{mf} value and the existence of bubbles rising very quickly through the bed [23]. Handling the CNT particles in a gas−solid fluidized bed encounters difficulty arising from the cohesive forces between the particles, more potent than the hydrodynamic forces applied by the fluid medium. The aggregation of primary particles in the fluidized bed depends on the inter-particle interactions, which, in turn, are a function of the primary particle size and gas velocity. The CNT aggregates size, the number of particles embedded in the aggregates, and aspect ratio increase with increasing gas velocity, although the roundness and the solidity decrease. The variations of the aggregates sizes and shape factors with gas velocity are affected by the initial mean particle size due to differences in factors contributing to the aggregate formation, such as physical entanglement between large CNT particles and the cohesive forces

between fine particles and separated nanotubes [24].

To improve the fluidization behavior of ABF-type powders, the mixing of hard-to-fluidized NPs with secondary fluidizable materials can be applied as a cost-effective and straightforward enhancement method compared to the expensive external assisted methods [19,20]. The NPs with better fluidization behavior, such as hydrophobic silica, are the most common auxiliary additives to enhance the fluidization ability of hard-to-fluidized NPs [20]. By adding the optimized amounts of the mentioned assistant materials, U_{mf} will decrease while the bed expansion increases [19,20,23,25–27].

It has been shown that CNTs tend to form agglomerates with multi-staged agglomerate structures, which results in the heterogeneous ABF behavior with a strong hysteresis in the wide range of gas velocities [28]. However, the homogenous fluidization of NPs, especially nano-scale and tremendously efficient sorbents, is undoubtedly required to facilitate the implementation of fluidized bed reactors in industrial applications. Then, promoting the fluidization of hard-to-fluidize CNT-based sorbents may play an essential role in improving their efficiency when utilized in a pilot or an industrial-scale fluidized bed reactor. Based on the performed literature review, little or no attention has been paid to assessing the fluidity of pure and chemically-modified CNT-based sorbents. Moreover, no efficient procedure has been proposed to improve their fluidizability.

This work mainly aimed at improving the fluidization ability of CNT-based sorbents, which will result in an increased gas−solid contact to promote the adsorption of CO_2 on their surface and, consequently, enhance the sorption efficiency of fluidized bed reactor. To this purpose, silica-coated amine-functionalized CNTs (MEA-Si-CNT) were firstly synthesized to promote the CO_2 sorption capacity. Scanning electron microscopy (SEM) and Fourier-transform infrared spectroscopy (FTIR) analyses were conducted to confirm the accuracy of the synthesis procedure. Thermogravimetric analysis (TGA) was also performed to verify the improved CO_2 capture capacity of the synthesized sorbent. Since the detailed hydrodynamic behavior of pure or chemically-modified CNTs during fluidization has been rarely reported, the fluidizability of pure and MEA-Si-CNTs were assessed in a lab-scale bed working at low gas velocities. Then, disparate mass percentages of silica NPs were physically mixed with both CNT-based sorbents to improve gas−solids contact efficiency. The fluidization performance was studied by the bed expansion ratio, pressure drop measurements across the bed at different gas velocities for calculating the U_{mf}, Richardson–Zaki (R–Z) equation to interpret fluidization behavior, and Romero and Johanson theory for predicting the fluidization quality through a combination of dimensionless groups.

2　Experimental

2.1　Materials and methods

Functionalized multi-walled CNTs (MWCNTs) containing carboxyl groups with primary particle size of 20–30 nm and 8 μm length, particle density of about 2200 kg·m^{-3}, and tapped bulk density of 102 kg·m^{-3} were purchased from Vira Carbon Nano materials company, Iran. Cetyl trimethyl ammonium bromide (CTAB, Merck), ethanol (99.7% purity, Hamoon Teb Markazi Co., Iran), aqueous ammonia (28%–30%, Merck), tetraethyl orthosilicate (Merck), ammonium nitrate (Merck), and industrial-grade MEA (Shazand petrochemical Co., Iran) were also used in this study. The MEA-Si-CNTs were synthesized based on the procedure described in the literature [29].

Hydrophobic SiO$_2$ NPs (Aerosil R972 from Evonik) with a primary particle diameter of 16 nm, particle density of 2200 kg·m^{-3}, and tapped bulk density of 50 kg·m^{-3} were chosen as additives to improve the fluidization characteristics of CNTs and MEA-Si-CNTs. To remove larger agglomerates of SiO$_2$ NPs, they first meshed through a 150 μm sieve. Then, small amounts including 2.5, 5, 7.5, and 10 wt% were added to pure and modified CNTs following the hand dry-mixing method for 30 min.

2.2　Fluidization experiments

The fluidization experiments were performed in a fluidized bed made of a glass column with an inner diameter (d_t) of 2.6 and 80 cm height oriented vertically. High purity N$_2$ (99.98%) fed the bed through a porous plate distributor installed at the bottom. A cyclone was used to collect and return the entrained particles. The bed height (H) was measured with a ruler tape stuck on the column wall. The pressure drop across the bed was measured with a manometer (pressure gauge, Wika) with two connection points: one just above the gas distributor and the other at the top of the column with a 70 cm distance from each other. The $H \cdot H_0^{-1}$ (H_0 is the initial bed height before the gas is fed to the bed) is the parameter that reveals the fluidization behavior of the sorbent. All the samples were prepared with the equivalent initial loading volume as an effect-less parameter for comparing their fluidity behavior. All fluidization tests were conducted at room temperature and atmospheric pressure.

2.3　Theoretical characterizations

The high $H \cdot H_0^{-1}$, which H_0 and H addressed to the bed heights at zero and the considered gas velocity, respectively, indicates homogeneity in their fluidity during the fluidization of materials. Additionally, U_{mf}, the lowest velocity at which the material commences to fluidize,

addresses the particles' cohesiveness [30]. Using the graphical method, U_{mf} can be calculated by the intersection between the line defined in the pressure drop versus velocity diagram at relatively low gas velocities (fixed bed region) and the horizontal line dictated by the constant pressure drop when the bed is fully fluidized at higher velocities [31].

To more deeply interpret the flowability performance of the samples, the R–Z equation [32] is applied in this study. The R–Z equation is primarily developed for liquid−solid systems when the inter-particle forces were insignificant [33]. However, the modified version of this equation (which applies to NP agglomerates rather than individual NPs) can investigate the degree of particulate fluidization in gas–solid systems. The R–Z equation relates the inlet gas velocity (U_g) to the bed voidage (ε_b) and the terminal velocity (U_t) for an agglomerate as follows [23,30]:

$$U_g = U_t \times \varepsilon_b^n. \qquad (1)$$

The logarithmic form of Eq. (1) gives a linear equation as follows:

$$\text{Log } U_g = \text{Log } U_t + n\text{Log } \varepsilon_b, \qquad (2)$$

where U_g is the superficial gas velocity, n is the index of R–Z's equation, an indicator of the particles fluidization performance, and ε_b is calculated from Eq. (3):

$$\varepsilon_b = 1 - \frac{H_0}{H}(1 - \varepsilon_{b0}). \qquad (3)$$

According to [34], the value of the initial bed voidage (ε_{b0}) for NPs is in the range of 0.2–0.25. Therefore, a ε_{b0} value of 0.22 is selected for both CNT and SiO$_2$ NPs in the calculations. The n index value is obtained graphically by plotting log U_g against log ε_b. It is believed that the n index interprets the quality of fluidization behavior of NPs. Consequently, APF-type NPs present a relatively higher n index than the ABF ones, confirming the more homogenous fluidity of the latter. Based on previous investigations [19,23], an n index value of 5 is considered as the limit for the fluidity behavior.

Romero [35] presented a model to characterize the fluidization quality as either homogeneous or bubbling, based on experimental results from classical fluidized particles such as fluid catalytic cracking catalysts and hollow resins. The model relies on the value of a combination of dimensionless numbers. The dimensionless Π parameter includes the product of the fluid density ratio, the Reynolds (Re_{mf}) and Froude (Fr_{mf}) numbers at minimum fluidization, and the bed height to bed diameter ratio as follows [36]:

$$\Pi = Fr_{mf}Re_{mf}\frac{\rho_a - \rho_g}{\rho_g}\frac{H_{mf}}{d_t}\begin{cases} < 100\text{APF} \\ > 100\text{ABF} \end{cases}. \qquad (4)$$

The Re_{mf} and Fr_{mf} numbers can be calculated as:

$$Re_{mf} = \frac{\rho_a d_a U_{mf}}{\mu}, \qquad (5)$$

$$Fr_{mf} = \frac{U_{mf}^2}{d_a g}. \tag{6}$$

By using Eqs. (5) and (6) into Eq. (4), the following expression for the Π parameter is obtained:

$$\Pi = \frac{\rho_a U_{mf}^3}{\mu g} \frac{\rho_a - \rho_g}{\rho_g} \frac{H_{mf}}{d_t}, \tag{7}$$

where, μ and ρ_g are the viscosity and density of N_2, respectively ($\mu = 1.77 \times 10^{-5}$ Pa·s^{-1}, $\rho = 1.165$ kg·m^{-3}), ρ_a is the density of the agglomerates, which is considered equal to the bulk density ($\rho_a = 102.35$ kg·m^{-3}), g is the gravity acceleration ($g = 9.8$ m·s^{-2}), H_{mf} is the bed height at U_{mf} determined by visual observation, d_t is the bed diameter ($d_t = 2.6$ cm), and d_a is the average size of the agglomerates.

2.4 Experimental characterization

Cyclic CO_2 adsorption/regeneration activity of pure CNT and MEA-Si-CNT was assessed in a TGA performed at atmospheric pressure. The samples were degassed at 120 °C for 1 h in the TGA pan under N_2 with an 80 mL·min^{-1} flow rate. By supplanting N_2 with a gas flow containing 15 vol% CO_2/85 vol% N_2, the CO_2 uptake stage of samples was performed for 1 h at 25 °C. Regeneration stage tests were conducted following the CO_2 uptake test, at 125 °C in a N_2 flow rate of 80 mL·min^{-1} for 30 min.

The presence of chemical compounds and functional groups of amine and silica onto the CNTs surface was investigated via FTIR using a TENSOR 27 FTIR instrument from Brucker Co. The morphologies of pure and MEA-Si-CNTs before and after mixing with hydrophobic SiO_2 NPs were analyzed by SEM using a FEI Quanta200 microscope.

3 Results and discussion

3.1 Characterizations of pure CNT and MEA-Si-CNT

To identify the effective hydroxyl and carboxyl functional groups in the structure of CNT and also to evaluate the underwent morphological changes of CNT after modification such as the formation of the silica layer and amine groups on its surface, the FTIR spectra patterns of pure CNT and MEA-Si-CNT are displayed in Fig. 1. According to FTIR spectra of pure CNT, the characteristic band of 3436 cm^{-1} is assigned to the presence of hydroxyl group on the CNT surface [37]. The peak at 2860 cm^{-1} can be attributed to the C–H bond's deformation vibration [9]. The characteristic band of carboxylate anion stretch mode is observed at 1560 cm^{-1} [38]. In the case of MEA-Si-CNT, FTIR spectra peak at 1064 cm^{-1}, addressed to the Si–O–Si bond, indicates the coating of CNTs with silica [39]. The peak at 3394 cm^{-1}, corresponding to –NH_2, proves the amine functionalization of CNTs [40]. A peak located at 2902 cm^{-1} is related to the –CH_2 group of CTAB surfactant, demonstrating the non-complete surfactant removal [41]. Additionally, the visible peak at 1651 cm^{-1} belongs to the –COOH groups. The appeared bands at 674 and 790 cm^{-1} indicate N–C≡O and Si–O skeletal fluctuations, respectively [29].

The surface morphology of pure CNT and MEA-Si-CNT via SEM micrographs is presented in Fig. 2. The comparison of Figs. 2(a) and 2(b) reveals that CNTs diameter increases from ~30–40 nm to ⩾ ~250 nm, derived from the formation of a thick layer of silica on their surface. The main reason for the final morphology of MEA-Si-CNT is the fast hydrolysis reaction of tetraethyl orthosilicate (TEOS) during the sorbent synthesis, which results in the non-uniform formation of the thick silica layer on CNTs. Therefore, it is impossible to report a specific particle size for the MEA-Si-CNT sorbent; however, the range of 60–450 nm can be estimated based on the SEM results. It should also be mentioned that MEA-Si-CNT particles form agglomerates with diameters greater than 10 μm. The SEM micrograph of MEA-Si-CNT indicates CNTs' structure resistance to change after the chemical modification, attributed to the high strength of CNTs.

3.2 Sorption performance of pure CNT and MEA-Si-CNT

CO_2 uptake capacity (mmol adsorbed CO_2·g^{-1} of sorbent) of pure CNT and MEA-Si-CNT during five consecutive adsorption/regeneration cycles is presented in Table 1. Pure CNT indicates a negligible CO_2 adsorption capacity at 25 °C. This insignificant uptake mainly relates to the presence of impurities, including amorphous carbon, fullerenes, nano-scale graphite catalysts, iron, nickel, and cobalt metal catalysts in the structure of CNT [42]. By acidification, not only the impurities are eliminated, and oxygenated functional groups such as negative-charge carboxyl are bound on CNTs surface, but also the length and agglomeration rate of CNTs are reduced [43]. On the
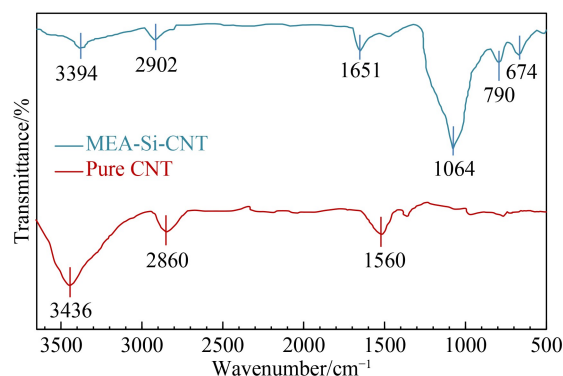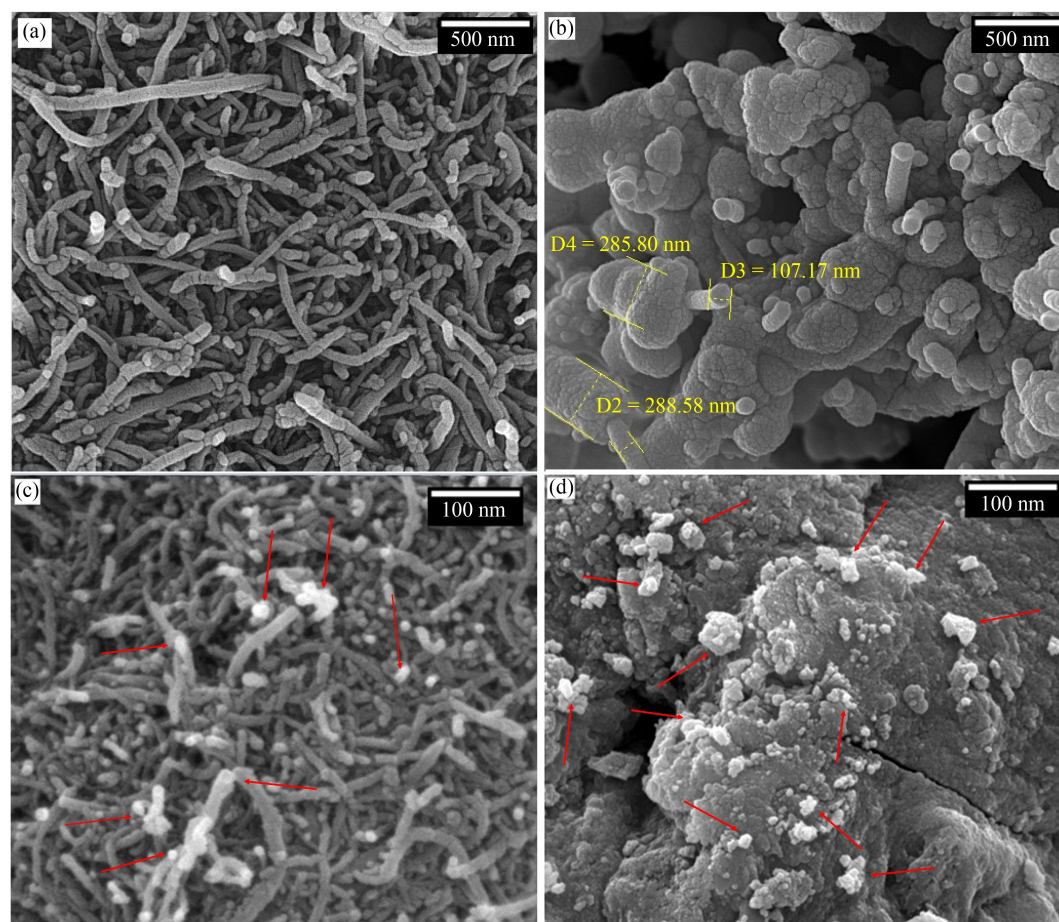

Fig. 1 FTIR spectra of pure CNT and MEA-Si-CNT.

Fig. 2 SEM micrographs of (a) pure CNT, (b) MEA-Si-CNT, (c) pure CNT + 10 wt% SiO_2 NPs, and (d) MEA-Si-CNT + 7.5 wt% SiO_2 NPs.

Table 1 CO_2 sorption capacity of pure CNT and MEA-Si-CNT during 5 consecutive adsorption/regeneration cycles [a]

Sorbent	CO_2 sorption capacity/(mmol $CO_2 \cdot g^{-1}$ of sorbent)				
	1st cycle	2nd cycle	3rd cycle	4th cycle	5th cycle
Pure CNT	0.032	0.026	0.023	0.021	0.020
MEA-Si-CNT	0.670	0.670	0.605	0.541	0.553

a) Adsorption at 25 °C for 1 h under 15 vol% CO_2/85 vol% N_2, regeneration at 125 °C for 1 h under N_2.

other hand, adding silica and MEA to the CNT matrix is conducive to improved sorption performance substantially so that ~25 times higher amount of CO_2 is adsorbed by MEA-Si-CNT compared to pure CNT during five multicycles. Due to the modification of the electrostatic interactions between negatively charged CNTs with CTAB (surfactant) cation, hydrophobic CNTs dissolve in water. Hydrolysis of injected TEOS into the solution produces polyanion silicate that enhances the high-surface mesosilica layer growth by electrostatic and hydrogen bonding with the cationic surfactant, increasing CNTs surface and pores to take a higher amount of amines [9,44]. The possible adsorption mechanisms can be classified as either physical or chemical depending on the type of forces established between the adsorbed material and the adsorbent. In physisorption, the target

molecules are attracted to the surface of pore walls within a high surface-area sorbent by van der Waals forces. In chemisorption, the target gas undergoes a covalent chemical reaction bind to specific sites on the sorbent [45]. The phenomenon of CO_2 capture by silica-coated CNTs relies on physical interactions; however, after amine functionalization, the chemical interaction between the CO_2 as a Lewis acid and primary amine sites on the adsorbent is noticed to some extent. It is worth noting that a part of the CO_2 adsorption on amine-functionalized CNT adsorbents is chemical, but physical adsorption is predominant. The CO_2 capture capacity of MEA-Si-CNT decreased when the temperature increased from 25 to 80 °C, indicating the exothermic nature of the process and, thus, the predominance of physical adsorption, similarly to other work published in the literature [46].

The reaction rates in fluidized beds, limited by the performance of gas−solids contact and mass/heat transfer between gas and particles sequentially, are not addressed in the TGA. Thus, research on the fluidizability of CNT-based sorbents is required to facilitate the implementation of nano-sorbents in industrial units.

3.3 Fluidizability of pure CNT and MEA-Si-CNT

The fluidization results of pure CNTs, in the gas velocity range of ~0.5–4.5 cm·s^{-1} are presented in Fig. 3. As it can be observed from Fig. 3(a), the $H·H_0^{-1}$ at a gas velocity of ~4 cm·s^{-1} reaches ~2.18. This low $H·H_0^{-1}$ associated with the non-uniform fluidization behavior can be

ascribed to the prevalence of inter-particle attractions between the CNT particles. The formation of stable narrow gas channels through the bed hinders the expansion of the bed and leads to an inefficient contact between the gas and fluidized particles. With the increase in the gas velocity, the bed starts to fluidize, although the particles vacillate irregularly on the bed surface. It is worth noting that typical forces considered in fluidized beds are drag, gravity, and collision forces as separating forces and van der Waals as adhesion force. The internal van der Waals force keeps the particles together in the agglomerate form, while external forces cause the agglomerates to break up. If external forces are more potent than the internal, they can break the agglomerates
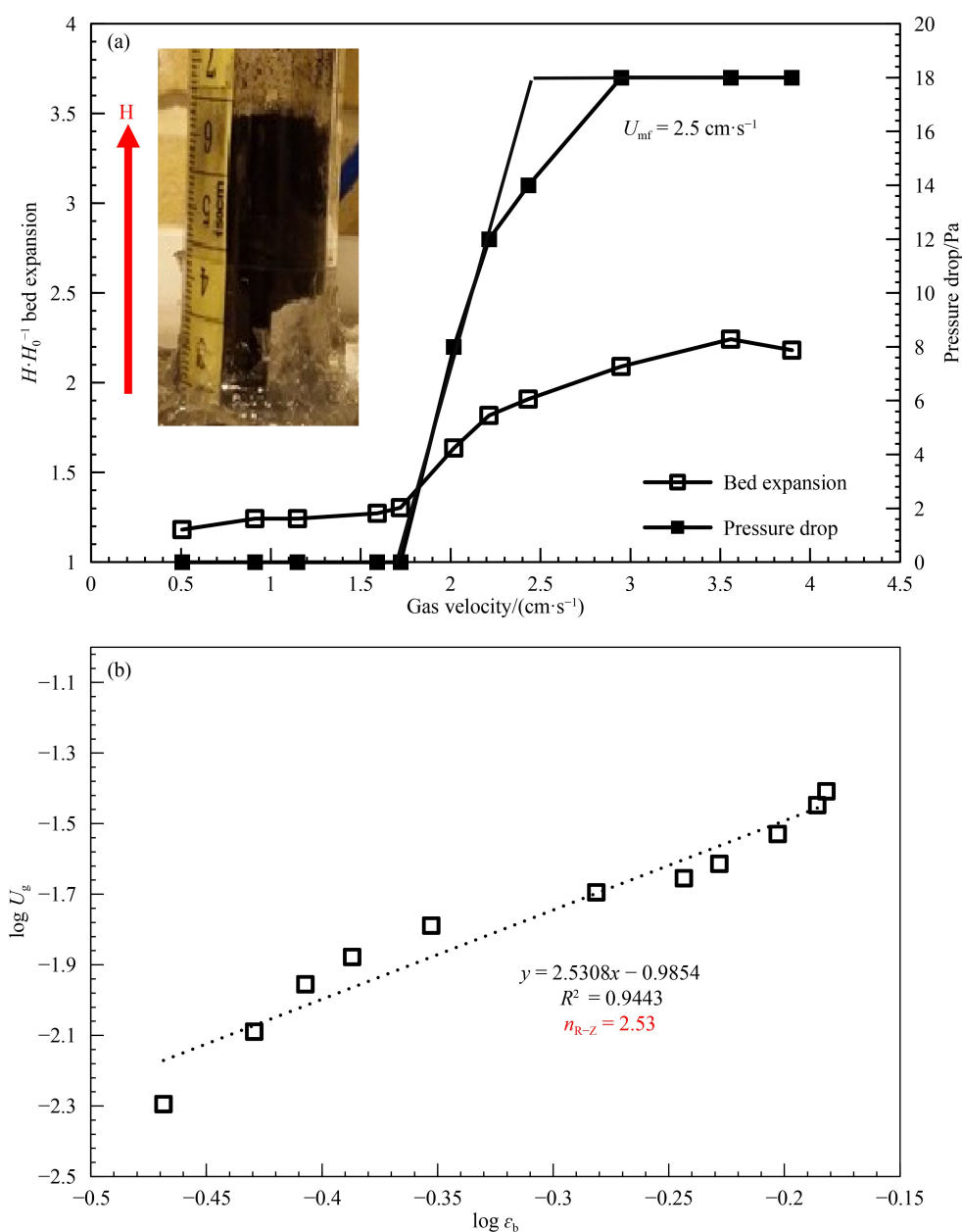

Fig. 3 (a) Bed expansion and measured pressure drop curves for pure CNT; (b) plot of log U_g against log ε_b according to the linear form of the R–Z's equation for pure CNT.

of particles into smaller pieces with better fluidity [30]. It happens when more drag force imposes on the particles by raising the upward-flowing gas velocity, which is why higher bed expansion with increased U_g. The driving force applied by an U_g above 2.5 cm·s^{-1} overcomes the weight of the particles.

Accordingly, the measured U_{mf} is around 2.5 cm·s^{-1}, confirmed by calculation using the pressure drop diagram (see Fig. 3(a)). At gas velocities higher than U_{mf}, high inter-particle adhesion forces still hinder the complete expansion of the bed, i.e., a bed expansion of ~2.24 at a gas velocity around 3.5 cm·s^{-1}, forming stable macro-sized agglomerates that consequently leads to the heterogeneous fluidization. Based on visual observations, the smooth decrease in the bed expansion of fluidized particles at gas velocities well above 3.5 cm·s^{-1} relates to the appearance of gas bubbles through the bed. This behavior corresponds to agglomerate bubbling fluidization-ABF behavior, characterized by heterogeneous fluidity with the arrival of bubbles throughout the bed, low bed expansion (~2.2 at a gas velocity of ~4 cm·s^{-1}), and the high U_{mf} value (~2.5 cm·s^{-1}). The fluidization characteristics of pure CNT are summarized in Table 2.

Figure 3(b) presents the R–Z logarithmic plot for pure CNT. As can be seen, the correlation coefficient for the linear fitting of the experimental data is above 0.9, which indicates that the fluidized system obeys the R–Z equation very well. The R–Z n index of 2.53 is calculated for pure CNT, which is proof for the ABF fluidization behavior of this sample and is in satisfying accordance with visual observations, bed expansion curve, and obtained U_{mf} value from pressure drop diagram.

According to the previously indicated values of the parameters, a Π matter of 1388 is calculated for pure CNT, indicative of ABF behavior and in correspondence with the estimated n index value. As demonstrated, functionalizing the surface of the support materials by modification with amine groups leads to improved CO_2 sorption performance. To this point, the fluidity performance of MEA-Si-CNTs is also investigated in the fluidized bed setup. The formation of visible large agglomerates of the sorbent at the bottom of the bed causes severe gas channels and cracks. Attempting fluidization at high gas velocities still causes the development of gas channels due to inefficient gas−solid contact. Visual observation reveals that an unusual fountain phenomenon develops with the increase in gas velocity

up to 4.5 cm·s^{-1}. Accordingly, the bed height remains almost fixed upon fluidization due to the cohesive nature of MEA-Si-CNT and the strong inter-particle forces. The cohesive forces in the MEA-Si-CNT bed cannot be overcome by manually shaking and imposing vibration on the bed. As a result, no homogeneous fluidization occurs at high gas velocities (4.5 m·s^{-1}), and ABF behavior is still predominant for the MEA-Si-CNTs, leading to the formation of large aggregates. The presence of electrical charge on the surface of MEA-Si-CNT particles due to the chemical modification can be the reason for their tendency to form large agglomerates.

3.4 Fluidizability of binary mixtures of pure CNT or MEA-Si-CNT + SiO$_2$ NPs

Amjadi et al. [25] indicated that adding easy-fluidizable NPs to the nano-scale powders decreases inter-particle cohesive forces and inhibits the development of large compact aggregates during fluidity leading to more homogenous fluidization. To improve the fluidity of hard-to-fluidize pure CNT and MEA-Si-CNT, these sorbents were mixed with differential weigh percentages of SiO$_2$ NPs.

3.4.1 Fluidizability of pure CNT + SiO$_2$ NPs

Figure 4 presents the bed expansion and pressure drop curves for disparate binary mixtures of CNT + SiO$_2$. It is apparent from Fig. 4(a) that by adding SiO$_2$ NPs to the bed consisting of CNTs, the $H \cdot H_0^{-1}$ increases substantially, which enhances the fluidization quality. For example, at the U_g of 3.5 cm·s^{-1}, the $H \cdot H_0^{-1}$ for binary mixtures of CNT + SiO$_2$ with silica weight percentages of 2.5%, 5%, 7.5%, and 10% reaches up to 2.78, 3.02, 3.19, and 3.43, respectively. In contrast, the pure CNT demonstrates a value of 2.24. The upper surface fluctuations also disappear by adding silica NPs to the bed of pure CNT. For the binary mixtures of CNT + 2.5 and 5 wt% SiO$_2$, based on the visual observation, although the channels form at a gas velocity of 1.5 cm·s^{-1}, the bed starts to fluidize at gas velocities of 2.1 and 1.9 cm·s^{-1}, respectively. Table 2 also constitutes the fluidity properties of binary mixtures of pure CNT + SiO$_2$. U_{mf} values calculated from the pressure drop curves of CNT + 2.5 and 5 wt% SiO$_2$ concede the onset of fluidization at 2.1 and 1.9 cm·s^{-1}, respectively (see Figs. 4(b) and 4(c)). By increasing the

Table 2 Fluidity characteristics of pure CNT and binary mixtures of pure CNT + SiO$_2$ NPs

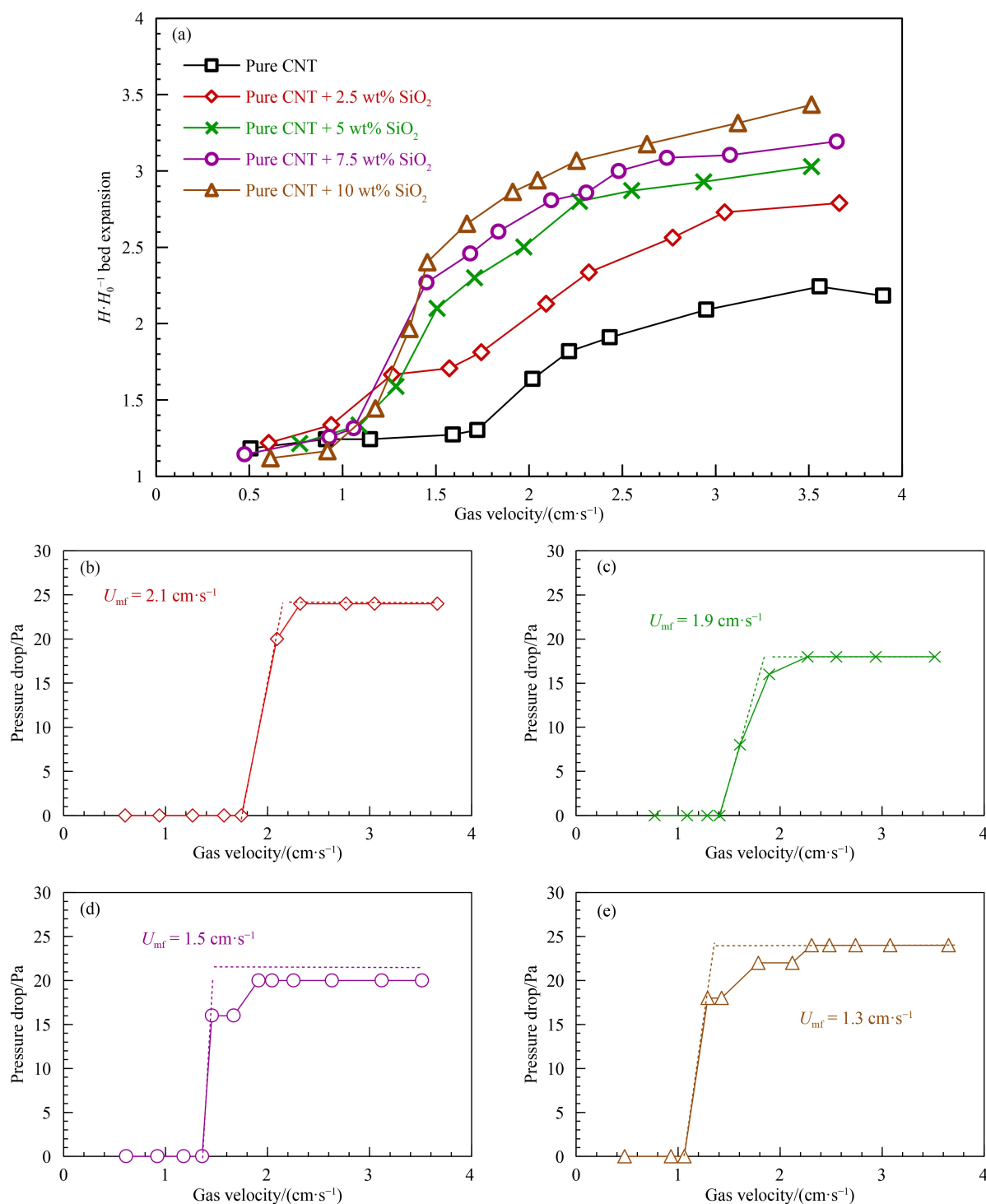| Sorbent	SiO$_2$ NPs/(wt%)	ρ_a/(kg·m^{-3})	H_{mf}/cm	U_{mf}/(cm·s^{-1})	n Index	Π	Fluidity behavior
Pure CNT +	0	102.35	4.5	2.5	2.5	1388	ABF
	2.5	80.7	4.2	2.1	2.8	475	ABF
	5	69.4	4.2	1.9	3.8	259	ABF
	7.5	57.5	4	1.5	5.2	83.2	APF
	10	46.8	3.9	1.3	6.5	35.7	APF

Fig. 4 (a) Bed expansion curves for binary mixtures of pure CNT + SiO$_2$ NPs and measured pressure drop curves for pure CNT + SiO$_2$ NPs with silica weight percentages of (b) 2.5 wt%, (c) 5 wt%, (d) 7.5 wt% and (e) 10 wt%.

SiO$_2$ NPs loading in the mixture, the beginning of the fluidization shifts to slightly lower gas velocities so that the U_{mf} values for the CNT + SiO$_2$ mixtures with silica weight percentages of 7.5% and 10% are 1.5 and 1.3 cm·s^{-1}, respectively (see Figs. 4(d) and 4(e)). The lower bed expansions of the CNT + SiO$_2$ mixtures with the lower loadings of silica NPs (i.e., 2.5 and 5 wt%) may be attributed to the cohesive inter-particle forces, which

remain even by the addition of SiO$_2$. The fine gas channels formed at low gas velocity for pure CNT mixed with 7.5 wt% SiO$_2$ NPs rapidly disappear at gas velocities higher than 1.5 cm·s^{-1}. More increase in the SiO$_2$ NPs loading does not present substantial variations so that the bed height remains relatively constant. The more appropriate fluidization quality along with a smooth bubble-free homogeneous bed for the mixtures of CNTs +

higher than 7.5 wt% SiO_2 NPs relates to the further reduction in the inter-particle adhesion forces between CNT NPs, following the visual observations. All the obtained results suggest that SiO_2 NPs are sufficient auxiliary materials to improve the fluidity of hard-to-fluidize pure CNTs. As a significant outcome, the easy-fluidizable silica agglomerates become the carriers of CNT particles, resulting in an improved fluidization behavior. These results are in high-grade conformity with the visual observations where the binary mixtures of CNT + 7.5 and 10 wt% SiO_2 NPs present bubble-free uniform fluidity.

Figure 5 shows pictures of the bed during fluidization at a constant gas velocity of ~3.5 cm·s^{-1} for increasing SiO_2 content in the CNT + SiO_2 NPs binary mixtures. As it is visible, in addition to higher bed expansion, the gas channels formed during fluidization are circumvented after adding 7.5 and 10 wt% SiO_2 NPs. The SEM of CNT + 10 wt% SiO_2 is presented in Fig. 2(c). As can be seen, the silica NPs, indicated by the red arrows in Fig. 2(c), are distributed between the CNTs. It can be inferred that strong electrostatic forces of attraction developed at the contact points between the SiO_2 NPs and CNT particles due to contact charging [19,20,23,25,26]. The easy-fluidizable SiO_2 NPs become carriers of the CNT particles, which improves the fluidity behavior. Additionally, the improvement of the CNT fluidity may be attributed to the decrease of the inter-particle adhesion forces between the CNT particles, as will be discussed in Section 3.5.

The plots of log U_g against log ε_b to calculate the R–Z n index for the binary mixtures of CNT and SiO_2 with silica weight percentages of 2.5%, 5%, 7.5%, and 10% are

illustrated in Fig. 6. It should be mentioned that the calculated correlation coefficients for the linear fittings are all above 0.9, indicating that the fluidized systems obey the R–Z equation varies considerably (see Figs. 6(a–d)). The listed values of the n index in Table 2 are 2.8, 3.85, 5.22, and 6.5 for pure CNT + 2.5, 5, 7.5, and 10 wt% SiO_2 NPs, respectively. The calculated n index value of pristine CNTs is 2.5. It means that the n index increases by mixing CNTs with disparate mass percentages of SiO_2 NPs. Besides, further increasing the mass percentage of added SiO_2 NPs results in higher R–Z n index values. According to the calculated n index for binary mixtures of pure CNT + SiO_2 NPs, the fluidity performance of CNT + 7.5 and 10 wt% SiO_2 NPs can be characterized with APF fluidization behavior, in high-level conformity with visual observations, the predicted U_{mf}, and the obtained $H \cdot H_0^{-1}$. It is worth mentioning that, among these binary mixtures, CNT + 10 wt% SiO_2 NPs adsorbent shows the lowest U_{mf} and the maximum $H \cdot H_0^{-1}$, alongside the highest R–Z n index value.

To interpret the flowability behavior of CNTs mixed with 2.5, 5, 7.5, and 10 wt% SiO_2 NPs, Π values are also calculated by Eq. (7). According to the reported data in Table 2, Π values of 475, 259, 83.2, and 35.7 are calculated for binary mixtures of CNT + 2.5, 5, 7.5, and 10 wt% SiO_2 NPs, respectively. It can be concluded that the calculated Π values confirm the measured n index, U_{mf}, and $H \cdot H_0^{-1}$. In this regard, the Π values of binary mixtures of CNT + 7.5, 10 wt% SiO_2 NPs, which exhibited the n indexes above 5, high $H \cdot H_0^{-1}$ and low U_{mf}, are below 100 (83.2 and 35.7, respectively), confirming their APF behavior.
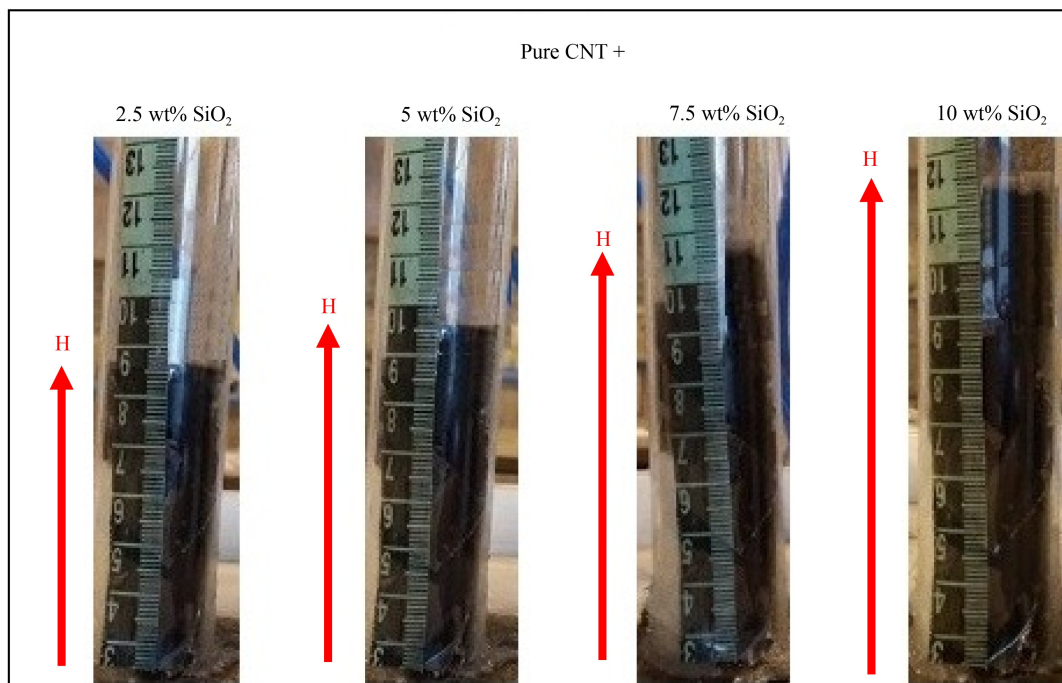

Fig. 5 Bed expansion setup pictures for binary mixtures of pure CNT + SiO_2 NPs fluidized in dry N_2 at a gas velocity of ~3.5 cm·s^{-1}.
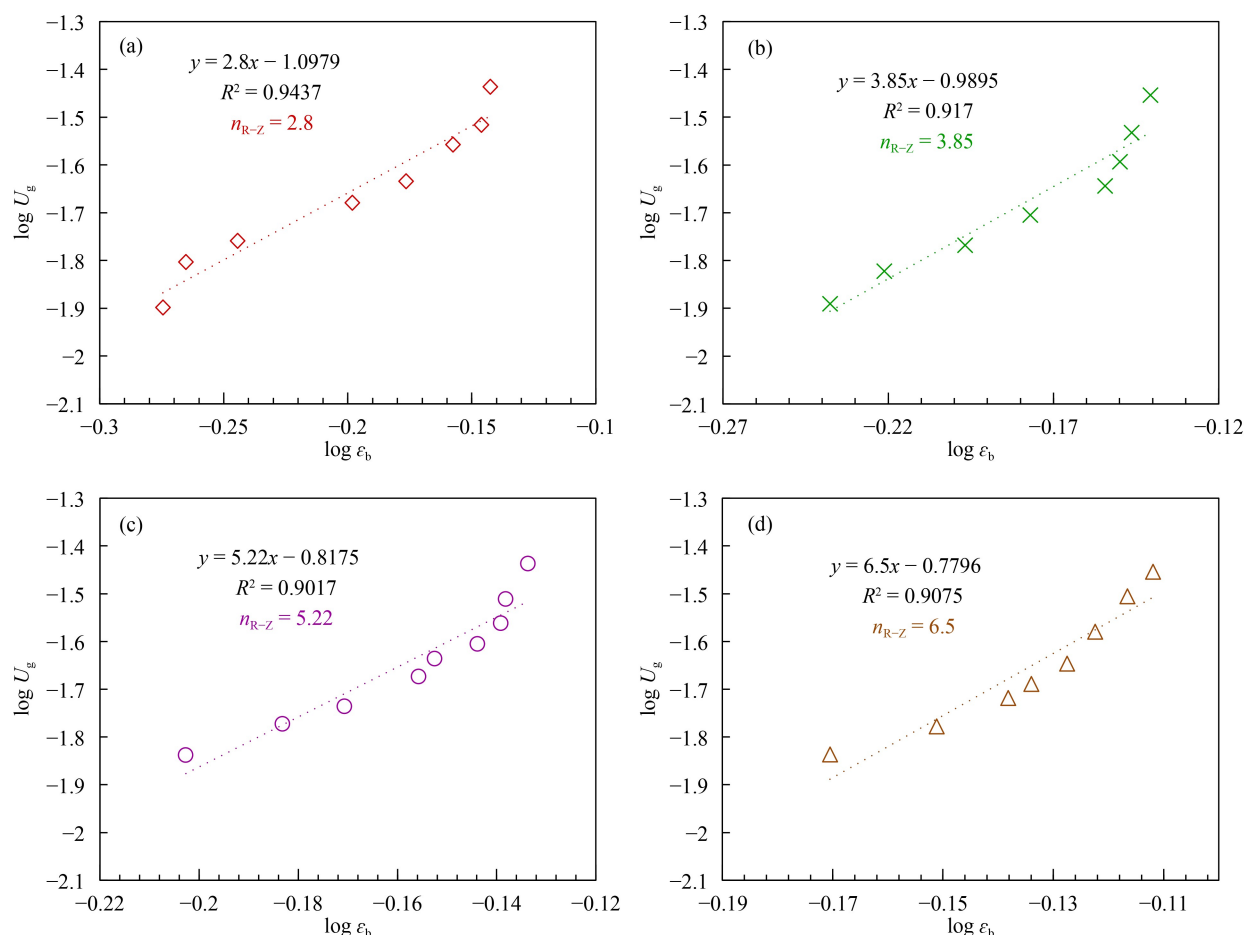
Fig. 6 Plot of $\log U_g$ against $\log \varepsilon_b$ for pure CNT + (a) 2.5 wt%, (b) 5 wt%, (c) 7.5 wt% and (d) 10 wt% SiO_2 NPs.

3.4.2 Fluidizability of MEA-Si-CNT + SiO_2 NPs

In addition to pure CNT, to improve the fluidizability of MEA-Si-CNT particles, several fluidization experiments are similarly performed by mixing with 2.5, 5, and 7.5 wt% of fluidizable silica NPs under low U_g in the range of 0.5–4.5 cm·s^{-1}. Accordingly, the $H \cdot H_0^{-1}$ and pressure drop curves for the disparate mixtures of MEA-Si-CNT + SiO_2 NPs fluidized by N_2 are illustrated in Fig. 7, as shown in Fig. 7(a), no significant improvement in the fluidity of MEA-Si-CNT + 2.5 wt% SiO_2 NPs occurs. The $H \cdot H_0^{-1}$ reaches only ~1.6 at a gas velocity of 3 cm·s^{-1}. Visual observations also reveal the appearance of channeling, rapid fluctuations of the bed surface, and the formation of large agglomerates at the bottom of the bed. At higher gas velocities, even though the $H \cdot H_0^{-1}$ increases to ~2.9 at a gas velocity of 4.3 cm·s^{-1}, an abnormal fountain phenomenon appears, and NP agglomerates fluidize heterogeneously. As shown in Fig. 7(b), a value of U_{mf} ~3.3 cm·s^{-1} is obtained for MEA-Si-CNT + 2.5 wt% SiO_2 NPs, indicating the ABF behavior of this binary mixture. Comparison of the obtained results reveals a greater enhancement in the fluidity of pure CNT by adding 2.5 wt% of SiO_2 NPs contrary to MEA-Si-CNT even though both samples follow an ABF behavior. It is

in conformity with the lower U_{mf} calculated for pure CNT + 2.5 wt% SiO_2 NPs (2.1 cm·s^{-1}).

It is found that raising the amount of added SiO_2 NPs from 2.5 to 7.5 wt% leads to the decrease of U_{mf} values from 3.3 to 1.2 cm·s^{-1} (see Figs. 7(b–d)). Accordingly, the $H \cdot H_0^{-1}$ at a gas velocity of ~3.3 cm·s^{-1} increases from 2.3 to ~3.9 when the amount of added SiO_2 NPs raises from 2.5 to 7.5 wt%. These results demonstrate that mixing 5 and 7.5 wt% of SiO_2 NPs with MEA-Si-CNTs favors the development of APF behavior, the main clue for a homogeneous, smooth, bubble-less, and durable liquid-like bed. This improvement is ascribed to the promoted deagglomeration by reducing the sticking tendency and adhesion forces between the NPs.

Figure 8 illustrates the bed expansion trend with increasing mass percentage of added SiO_2 NPs to MEA-Si-CNT when the inlet gas passed through the bed at a velocity of about 3.5 cm·s^{-1}. It is observed that the height of the bed increases with increasing the mass percentage of mixed SiO_2 NPs from 2.5 to 7.5 wt%. The SEM micrograph taken for MEA-Si-CNT mixed with 7.5 wt% silica NPs is presented in Fig. 2(d). The SiO_2 NPs are distributed between the MEA-Si-CNT particles, as indicated by the red arrows. The distribution of silica NPs between MEA-Si-CNT particles prevents the agglomeration phenomenon,

which causes the improvement of MEA-Si-CNT fluidity.

The plots of log U_g against log ε_b for the binary mixtures of MEA-Si-CNT and SiO_2 with silica weight percentages of 2.5%, 5%, and 7.5%, are presented in Fig. 9. As can be seen, the R–Z model fitting based on the fluidity characteristics shows the linear trend for all the mixtures of MEA-Si-CNT + SiO_2, as illustrated in Figs. 9(a–c). The fluidization characteristics of binary mixtures of

MEA-Si-CNT + SiO_2 NPs are presented in Table 3. The obtained results demonstrate the increase of n index values from 1.04 to 5.3 and 7.7 when the amount of added SiO_2 NPs raises from 2.5 to 5 and 7.5 wt%, respectively. The APF behavior of MEA-Si-CNT + 5 and 7.5 wt% SiO_2 NPs is confirmed by the R–Z n index values higher than 5. Among all the evaluated mixtures, the highest n index (7.7) is obtained in the case of MEA-
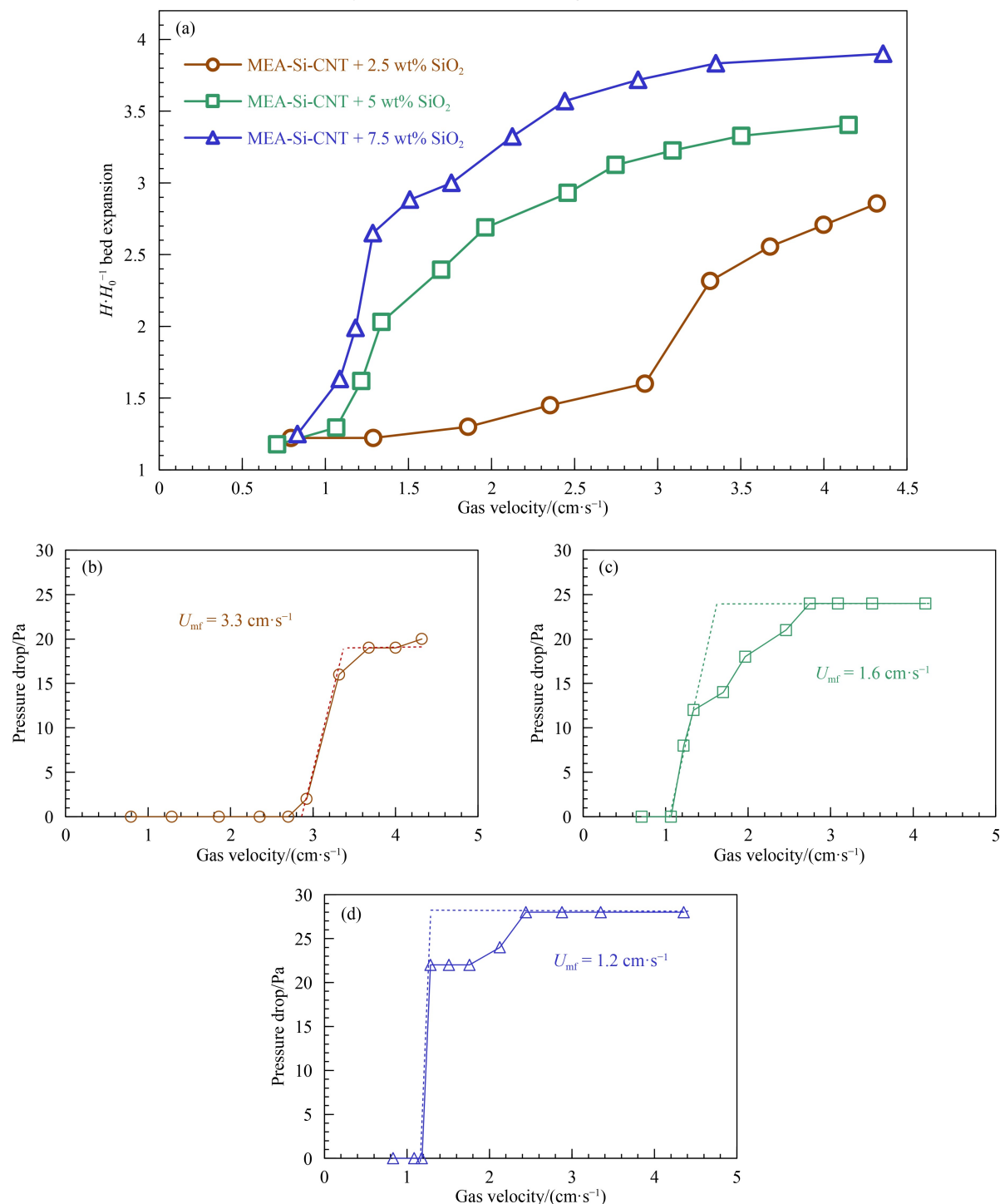

Fig. 7 (a) Bed expansion curves for binary mixtures of MEA-Si-CNT + SiO_2 NPs and measured pressure drop curves for mixtures of MEA-Si-CNT+ SiO_2 NPs with silica weight percentages of (b) 2.5 wt%, (c) 5 wt%, and (d) 7.5 wt%.
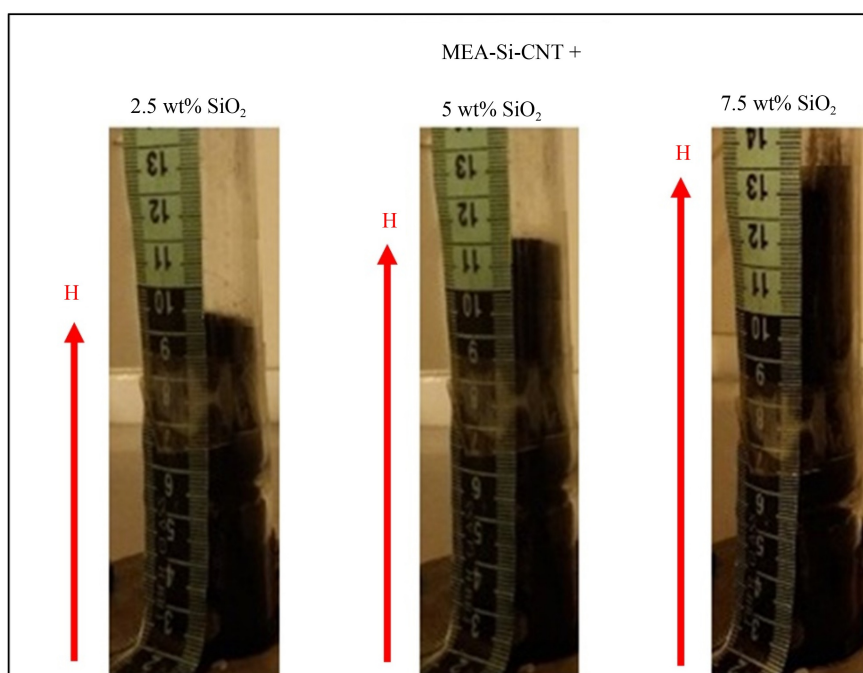
Fig. 8 Bed expansion pictures of mixtures of MEA-Si-CNT + disparate weight percentages of SiO_2 NPs fluidized in dry N_2 at a gas velocity of ~3.5 cm·s^{-1}.
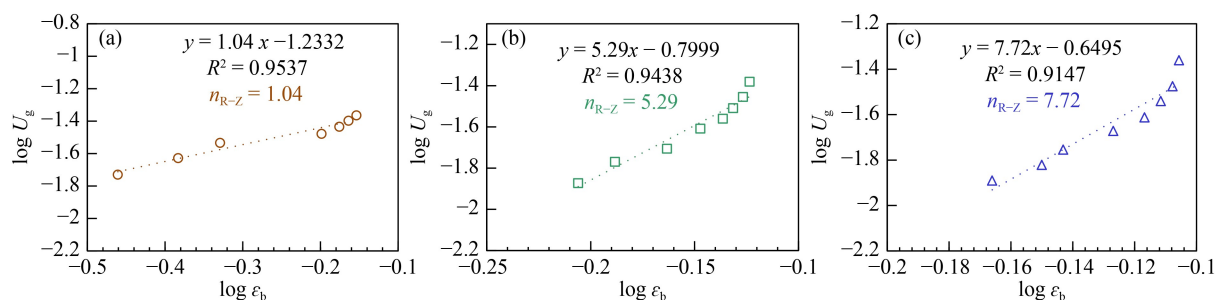

Fig. 9 Plot of log U_g against log ε_b for MEA-Si-CNT + (a) 2.5 wt%, (b) 5 wt% and (c) 7.5 wt% SiO_2 NPs.

Table 3 Fluidity characteristics of binary mixtures of MEA-Si-CNT + SiO_2 NPs

Sorbent	SiO_2 NPs/(wt%)	ρ_a/(kg·m^{-3})	H_{mf}/cm	U_{mf}/(cm·s^{-1})	n index	Π	Fluidity behavior
MEA-Si-CNT +	2.5	64.7	4.4	3.3	1.04	1237	ABF
	5	52.1	4.1	1.6	5.3	84.8	APF
	7.5	41.5	4	1.2	7.72	22	APF

Si-CNT + 7.5 wt% SiO_2 NPs, well above the n index (6.5) of pure CNT + 10 wt% of SiO_2 NPs.

Π values of 1237, 84.8, and 22 are calculated with Eqs. (4)–(7) for the mixtures of MEA-Si-CNT + 2.5, 5, and 7.5 wt% SiO_2 NPs, respectively. According to the calculated Π values of less than 100, it can be concluded that 5 and 7.5 wt% of added SiO_2 NPs are sufficient to change the fluidization performance of MEA-Si-CNT from ABF to APF behavior. There is a rewarding agreement between calculated Π values, R–Z n indexes, measured $H \cdot H_0^{-1}$, and U_{mf} of MEA-Si-CNT + 5 and 7.5 wt% SiO_2 NPs, all confirm the APF behavior.

To conduct a direct comparison between the fluidizability of binary mixtures with superior fluidity performance, bed expansion curves of pure CNT + 7.5 and 10 wt% SiO_2 and MEA-Si-CNT + 7.5 wt% SiO_2 are represented in Fig. 10. The bed expansion curves indicate the higher expansion of MEA-Si-CNT + 7.5 wt% SiO_2 NPs at virtually all gas velocities. For instance, the $H \cdot H_0^{-1}$ of 3.9 is reported for MEA-Si-CNT + 7.5 wt% SiO_2 NPs at a gas velocity of 3.5 cm·s^{-1}, roughly ~22% and ~14% higher than those of pure CNT + 7.5 ($H \cdot H_0^{-1}$ = 3.19) and CNT + 10 wt% SiO_2 ($H \cdot H_0^{-1}$ = 3.43), respectively. This superior fluidity performance of MEA-Si-CNT + 7.5 wt% SiO_2 NPs is also conceded by lower U_{mf} and Π values, as well as higher R–Z n index (see Fig. 10). Based on fluidity outcomes, it can be inferred that the effectiveness of adding SiO_2 NPs in improving the fluidity of non-fluidizable CNT-based sorbents is more noticeable in the case of MEA-Si-CNT. In addition, less

weight percentage of SiO_2 NPs is required to homogenize the fluidity of MEA-Si-CNT sorbent as ABF behavior compared to the pristine CNT. This superior performance can be attributed to the higher surface of MEA-Si-CNT, conducive to the more homogeneous dispersion of SiO_2 NPs on the sorbent surface and higher reduction in inter-particle adhesion. In this regard, MEA-Si-CNT presents more efficient fluidity after mixing with SiO_2 NPs compared to unmodified CNT.

3.5 Verification of outcomes

To verify the effectiveness of adding SiO_2 NPs to improve the fluidity of CNT particles, three different models, including the sandwich and the three-point contact models, and a proposed expression by Krupp [47], were assessed. The mentioned models assume that particles are spherical; although this assumption creates a minor error in the assertion of the van der Waals forces between cylindrical CNTs.

The sandwich contact model assumes that a fine guest particle is centered between two host particles and the van der Waals forces (F_{vdW}) for this system consist in the attraction between the two host particles ($F_{vdW,D-D}$) and the cohesion between the guest and host particles ($F_{vdW,d-D}$), calculated with the following equation [48]:

$$F_{vdW} = F_{vdW,D-D} + F_{vdW,d-D} = \frac{AD}{24(d+2z_0)^2} + \frac{AdD}{12z_0^2(d+D)}, \quad (8)$$

where A is the Hamaker constant, z_0 is the minimum surface distance between two particles (~0.4 nm), D and d are the diameters of the host and guest particles, respectively. When only pure MWCNTs exist, the expression of the van der Waals force calculation is simplified to:

$$F_{vdW,D-D} = \frac{AD}{24z_0^2}. \quad (9)$$

Comparing Eqs. (8) and (9) turns apparent that the van

der Waals force decreased by 21.89% with adding silica NPs, in agreement with the enhanced fluidization results.

The surface area coverage (SAC) of guest particles on host particles is not considered in the sandwich contact model. To investigate the effect of SAC and approach actual conditions, the three-point contact model assumes that the guest particles are distributed on the surface of the host particles, and the contact between two particles consists of three different stages depending on SAC. If SAC is very low, the host particles contact directly, and the host−host van der Waals force dominates. With increasing SAC to a particular value, two host particles depart from each other, and the guest–host interactions prevail. With a further increase of SAC (up to around 50%), the contact transforms to a guest–guest pattern. SAC can be determined from Eq. (10):

$$SAC = \frac{0.604}{1+2\left(\frac{D}{d}\right)} \times 100\%. \quad (10)$$

For our experiment, SAC was estimated as 14.64%, so the guest–host van der Waals force is dominant and can be calculated through Eq. (11):

$$F_{vdW,guest-host} = \frac{Ad}{4z_0^2} + \frac{A}{24D\left[\sqrt{\left(1+\frac{d}{D}\right)^2 - \frac{0.604}{SAC}\left(\frac{d}{D}\right)^2} - 1\right]^2}. \quad (11)$$

Considering Eqs. (10) and (11), it was gained that van der Waals's force decreased by 35.94% with the addition of silica NPs. The third correlation for predicting the van der Waals force is the expression of Krupp:

$$F_{cw} = \frac{h\omega R}{8z_0^2}, \quad (12)$$

where $h\omega$ is the Lifshitz−van der Waals coefficient ($h\omega = 4\pi A/3$) and $R = R_1 R_2/(R_1+R_2)$ where R_1 and R_2 are
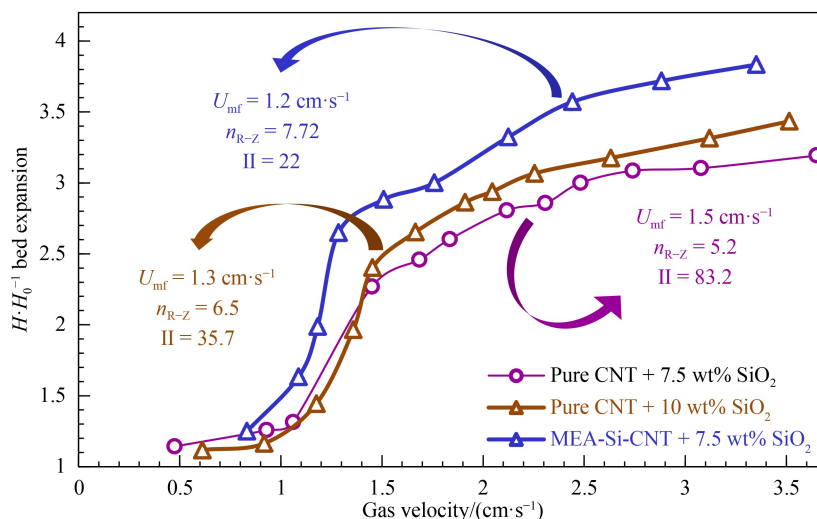

Fig. 10 Bed expansion curves for binary mixtures of pure CNT + 7.5 and 10 wt% SiO_2 and MEA-Si-CNT + 7.5 wt% SiO_2.

the radii of the two particles in contact, and according to Eq. (12), the van der Waals force decreased by 21.95% when adding silica NPs.

As mentioned previously, the main difficulty in fluidization arises because the inter-particle attractive forces are more potent than the particles' weight. These forces between the CNT and MEA-Si-CNT particles decrease by mixing with SiO_2 NPs. To this point, not only the adhesion forces will be overcome at lower gas velocities, but also no oversized agglomerates will form that hinder the gas−solid contact efficiency. Therefore, the fluidity of CNT particles will improve without channeling, bubbles, and big-size agglomerates.

Finally, it should be noted that, even though the temperature of ~25 °C was contemplated to study the fluidity of CNT-based sorbents in this work (adsorption conditions), the fluidization behavior of CNT and MEA-Si-CNT or their mixtures with SiO_2 NPs at a temperature of ~120 °C (regeneration conditions) will be the subject of the forthcoming research. Nonetheless, recent research has indicated fluidization performance improvement by raising the temperature. For instance, Xu et al. [49] reported that higher bed pressure drop, lower U_{mf}, and more homogeneous flowability were achieved for fine particles of groups Geldart A and C by increasing the temperature. Guo et al. [50] revealed the decrease in the U_{mf} of fluidized SiO_2 NPs when the bed temperature increased from ambient temperature to 800 °C. Furthermore, to address the effect of added SiO_2 NPs on the thermal stability and cyclic CO_2 capture capacity of CNT-based sorbents, the binary mixtures of CNT and MEA-Si-CNT with SiO_2 NPs must be subjected to multiple adsorption/regeneration cycles under conditions resembling those to be found in practice involving. The study on whether the presence of SiO_2 NPs in the samples plays a role in the capture efficiency during the cycles is in progress.

4   Conclusions

The main aims of this work are studying the CO_2 uptake activity and fluidity of CNT-based sorbents, including pure and MEA-Si-CNT, and then trying to improve the contact efficiency between gas−solids by adding disparate mass percentages of SiO_2 NPs as an auxiliary substance. The Flowability of both CNT-based sorbents and their binary mixtures with SiO_2 NPs is tested at ambient conditions by introducing an upward flow of N_2 to the bed. The following conclusions are achieved based on the experimental and theoretical results of this study:

(1) A novel MEA-Si-CNTs sorbent adsorbs ~25 times higher amount of CO_2 in comparison with unmodified MWCNT during 5 consecutive adsorption/regeneration cycles.

(2) Deficient $H \cdot H_0^{-1}$ with large bubbles and gas channels formation are observed for both sorbents, corresponding to the highly interparticle adhesion forces between their particles.

(3) Mixing pure CNT particles with disparate mass percentages of SiO_2 NPs results in a substantial increase of the gas−solids contact efficiency during the fluidization. The homogenous and bubbleless fluidity without gas channeling is achieved by mixing pure CNT with 7.5 wt% of SiO_2 NPs. The characteristics, including $H \cdot H_0^{-1}$ of 3.2 at the gas velocity of ~3.5 m·s^{-1}, R–Z n index of 5.2 > 5, Π value of 83.2 < 100, and the U_{mf} of 1.5 cm·s^{-1}, confirm the APF behavior.

(4) In the case of binary mixtures of MEA-Si-CNT + SiO_2 NPs, lab-scale fluidization experiments reveal the higher effectiveness of adding SiO_2 NPs on improving the flowability of MEA-Si-CNT particles and adding 5 wt% of fluidizable SiO_2 NPs to MEA-Si-CNT is sufficiently required to reach an entirely uniform, smooth, bubbleless, and homogenous APF behavior with the $H \cdot H_0^{-1}$ of 3.4 at the gas velocity of ~3.5 m·s^{-1}, R–Z n index of 5.3 > 5, Π value of 84.8 < 100 and the U_{mf} of 1.6 cm·s^{-1}.

(5) The main reason for this improvement in the fluidity performance of pure CNT and MEA-Si-CNT can be the distribution of fluidizable silica NPs between sorbent particles, which significantly reduces interparticle electrostatic force and hinders agglomeration of sorbent particles.

(6) Among all prepared binary mixtures, MEA-Si-CNT mixed with 7.5 wt% SiO_2 NPs possesses the most appropriate fluidity, even more efficient than those obtained by pure CNT + 7.5 and 10 wt% SiO_2 NPs.

References

1. Sattari F, Tahmasebpoor M, Valverde J M, Ortiz C, Mohammadpourfard M. Modelling of a fluidized bed carbonator reactor for post-combustion CO_2 capture considering bed hydrodynamics and sorbent characteristics. Chemical Engineering Journal, 2021, 406: 126762

2. Roussanaly S, Vitvarova M, Anantharaman R, Berstad D, Hagen

B, Jakobsen J, Novotny V, Skaugen G. Techno-economic comparison of three technologies for pre-combustion CO_2 capture from a lignite-fired IGCC. Frontiers of Chemical Science and Engineering, 2020, 14(3): 436–452

3. Hafeez S, Safdar T, Pallari E, Manos G, Aristodemou E, Zhang Z, Al-Salem S, Constantinou A. CO_2 capture using membrane contactors: a systematic literature review. Frontiers of Chemical Science and Engineering, 2021, 15(4): 720–754

4. Rama S, Zhang Y, Tchuenbou-Magaia F, Ding Y, Li Y. Encapsulation of 2-amino-2-methyl-1-propanol with tetraethyl orthosilicate for CO_2 capture. Frontiers of Chemical Science and Engineering, 2019, 13(4): 672–683

5. Xiao G, Xiao P, Hoadley A, Webley P. Integrated adsorption and absorption process for post-combustion CO_2 capture. Frontiers of Chemical Science and Engineering, 2021, 15(3): 483–492

6. Ghahramaninezhad M, Mohajer F, Shahrak M N. Improved CO_2 capture performances of ZIF-90 through sequential reduction and lithiation reactions to form a hard/hard structure. Frontiers of Chemical Science and Engineering, 2020, 14(3): 425–435

7. Xu Z, Jiang T, Zhang H, Zhao Y, Ma X, Wang S. Efficient MgO-doped CaO sorbent pellets for high temperature CO_2 capture. Frontiers of Chemical Science and Engineering, 2021, 15(3): 698–708

8. Xiao Q, Tang X, Liu Y, Zhong Y, Zhu W. Comparison study on strategies to prepare nanocrystalline Li_2ZrO_3-based absorbents for CO_2 capture at high temperatures. Frontiers of Chemical Science and Engineering, 2013, 7(3): 297–302

9. Nobarzad M J, Tahmasebpoor M, Imani M, Pevida C, Heris S Z. Improved CO_2 adsorption capacity and fluidization behavior of silica-coated amine-functionalized multi-walled carbon nanotubes. Journal of Environmental Chemical Engineering, 2021, 9(4): 105786

10. Heidari M, Tahmasebpoor M, Mousavi S B, Pevida C. CO_2 capture activity of a novel CaO adsorbent stabilized with (ZrO_2 + Al_2O_3 + CeO_2)-based additive under mild and realistic calcium looping conditions. Journal of CO_2 Utilization, 2021, 53: 101747

11. Gu C, Liu Y, Wang W, Liu J, Hu J. Effects of functional groups for CO_2 capture using metal organic frameworks. Frontiers of Chemical Science and Engineering, 2021, 15(2): 437–449

12. Ban Y, Zhao M, Yang W. Metal-organic framework-based CO_2 capture: from precise material design to high-efficiency membranes. Frontiers of Chemical Science and Engineering, 2020, 14(2): 188–215

13. Keller L, Ohs B, Lenhart J, Abduly L, Blanke P, Wessling M. High capacity polyethylenimine impregnated microtubes made of carbon nanotubes for CO_2 capture. Carbon, 2018, 126: 338–345

14. Lu C, Bai H, Wu B, Su F, Hwang J F. Comparative study of CO_2 capture by carbon nanotubes, activated carbons, and zeolites. Energy & Fuels, 2008, 22(5): 3050–3056

15. Mousavi S B, Zeinali Heris S. Experimental investigation of ZnO nanoparticles effects on thermophysical and tribological properties of diesel oil. International Journal of Hydrogen Energy, 2020, 45(43): 23603–23614

16. Seyedi S S, Shabgard M R, Mousavi S B, Heris S Z. The impact of SiC, Al_2O_3, and B_2O_3 abrasive particles and temperature on wear characteristics of 18Ni (300) maraging steel in abrasive flow

machining (AFM). International Journal of Hydrogen Energy, 2021, 46(68): 33991–34001

17. Mousavi S B, Zeinali Heris S, Estellé P. Viscosity, tribological and physicochemical features of ZnO and MoS_2 diesel oil-based nanofluids: an experimental study. Fuel, 2021, 293: 120481

18. Hu S, Liu X. Development of a hydrodynamic model and the corresponding virtual software for dual-loop circulating fluidized beds. Frontiers of Chemical Science and Engineering, 2021, 15(3): 579–590

19. Heidari M, Tahmasebpoor M, Antzaras A, Lemonidou A A. CO_2 capture and fluidity performance of CaO-based sorbents: effect of Zr, Al and Ce additives in tri-, bi- and mono-metallic configurations. Process Safety and Environmental Protection, 2020, 144: 349–365

20. Azimi B, Tahmasebpoor M, Sanchez-Jimenez P E, Perejon A, Valverde J M. Multicycle CO_2 capture activity and fluidizability of Al-based synthesized CaO sorbents. Chemical Engineering Journal, 2019, 358: 679–690

21. Atif R, Inam F. Reasons and remedies for the agglomeration of multilayered graphene and carbon nanotubes in polymers. Beilstein Journal of Nanotechnology, 2016, 7(1): 1174–1196

22. Yao W, Guangsheng G, Fei W, Jun W. Fluidization and agglomerate structure of SiO_2 nanoparticles. Powder Technology, 2002, 124(1): 152–159

23. Amjadi O, Tahmasebpoor M. Improving fluidization behavior of cohesive $Ca(OH)_2$ adsorbent using hydrophilic silica nanoparticles: parametric investigation. Particuology, 2018, 5: 52–61

24. Kim S W. Effect of particle size on carbon nanotube aggregates behavior in dilute phase of a fluidized bed. Processes, 2018, 6(8): 121

25. Amjadi O, Tahmasebpoor M, Aghdasinia H. Fluidization behavior of cohesive $Ca(OH)_2$ powders mixed with hydrophobic silica nanoparticles. Chemical Engineering & Technology, 2019, 42(2): 287–296

26. Rahimvandi Noupoor Y, Tahmasebpoor M. A novel internal assistance method for enhanced fluidization of nanoparticles. Korean Journal of Chemical Engineering, 2019, 36(8): 1377–1387

27. Tahmasebpoor M, Noupoor Y R, Badamchizadeh P. Fluidity enhancement of hard-to-fluidize nanoparticles by mixing with hydrophilic nanosilica and fluid catalytic cracking particles: experimental and theoretical study. Physics of Fluids, 2019, 31(7): 073301

28. Yu H, Zhang Q, Gu G, Wang Y, Luo G, Wei F. Hydrodynamics and gas mixing in a carbon nanotube agglomerate fluidized bed. AIChE Journal. American Institute of Chemical Engineers, 2006, 52(12): 4110–4123

29. Lee M S, Park S J. Silica-coated multi-walled carbon nanotubes impregnated with polyethyleneimine for carbon dioxide capture under the flue gas condition. Journal of Solid State Chemistry, 2015, 226: 17–23

30. Tahmasebpoor M, Ghasemi Seif Abadi R, Rahimvandi Noupoor Y, Badamchizadeh P. Model based on electrostatic repulsion and hydrogen bond forces to estimate the size of nanoparticle agglomerates in fluidization. Industrial & Engineering Chemistry Research, 2016, 55(50): 12939–12948

31. Shao Y, Li Z, Zhong W, Bian Z, Yu A. Minimum fluidization velocity of particles with different size distributions at elevated pressures and temperatures. Chemical Engineering Science, 2020, 216: 115555

32. Richardson J F, Zaki W N. Sedimentation and fluidisation: Part I. Chemical Engineering Research & Design, 1997, 75: S82–S100

33. Hakim L F, Portman J L, Casper M D, Weimer A W. Aggregation behavior of nanoparticles in fluidized beds. Powder Technology, 2005, 160(3): 149–160

34. Yang J, Zhou T, Song L. Agglomerating vibro-fluidization behavior of nano-particles. Advanced Powder Technology, 2009, 20(2): 158–163

35. Romero J B, Johanson L N. Factors affecting fluidized bed quality. Chemical Engineering Progress Symposium Series, 1958, 58: 28–37

36. Zhu C, Yu Q, Dave R N, Pfeffer R. Gas fluidization characteristics of nanoparticle agglomerates. AIChE Journal. American Institute of Chemical Engineers, 2005, 51(2): 426–439

37. Aljerf L. High-efficiency extraction of bromocresol purple dye and heavy metals as chromium from industrial effluent by adsorption onto a modified surface of zeolite: kinetics and equilibrium study. Journal of Environmental Management, 2018, 225: 120–132

38. do Amaral Montanheiro T L, Cristóvan F H, Machado J P B, Tada D B, Durán N, Lemes A P. Effect of MWCNT functionalization on thermal and electrical properties of PHBV/MWCNT nanocomposites. Journal of Materials Research, 2015, 30(1): 55–65

39. Hsu S C, Lu C, Su F, Zeng W, Chen W. Thermodynamics and regeneration studies of CO_2 adsorption on multi-walled carbon nanotubes. Chemical Engineering Science, 2010, 65(4): 1354–1361

40. Janakiraman N, Johnson M. Functional groups of tree ferns (Cyathea) using FTIR: chemotaxonomic implications. Romanian Journal of Biophysics, 2015, 25(2): 131–141

41. Sianipar M, Kim S H, Iskandar F, Wenten I G. Functionalized carbon nanotube (CNT) membrane: progress and challenges. RSC Advances, 2017, 7(81): 51175–51198

42. Pumera M, Ambrosi A, Chng E L K. Impurities in graphenes and carbon nanotubes and their influence on the redox properties. Chemical Science (Cambridge), 2012, 3(12): 3347–3355

43. Tasis D, Tagmatarchis N, Bianco A, Prato M. Chemistry of carbon nanotubes. Chemical Reviews, 2006, 106(3): 1105–1136

44. Yang J, Xu Y, Su C, Nie S, Li Z. Synthesis of hierarchical nanohybrid CNT@Ni-PS and its applications in enhancing the tribological, curing and thermal properties of epoxy nanocomposites. Frontiers of Chemical Science and Engineering, 2021, 15(5): 1–15

45. Berger A H, Bhown A S. Comparing physisorption and chemisorption solid sorbents for use separating CO_2 from flue gas using temperature swing adsorption. Energy Procedia, 2011, 4: 562–567

46. Sánchez-Zambrano K S, Lima Duarte L, Soares Maia D A, Vilarrasa-García E, Bastos-Neto M, Rodríguez-Castellón E, Silva de Azevedo D C. CO_2 capture with mesoporous silicas modified with amines by double functionalization: assessment of adsorption/desorption cycles. Materials, 2018, 11(6): 887

47. Krupp H, Sperling G. Theory of adhesion of small particles. Journal of Applied Physics, 1966, 37(11): 4176–4180

48. Zhu X, Zhang Q, Huang C, Wang Y, Yang C, Wei F. Validation of surface coating with nanoparticles to improve the flowability of fine cohesive powders. Particuology, 2017, 30: 53–61

49. Xu C, Zhu J-X. Effects of gas type and temperature on fine particle fluidization. China Particuology, 2006, 4(3−4): 114–121

50. Guo Q, Zhang J, Hao J. Flow characteristics in an acoustic bubbling fluidized bed at high temperature. Chemical Engineering and Processing, 2011, 50(3): 331–337